Three-State Ferroelastic Switching and Large Electromechanical Responses in PbTiO₃ Thin Films

Anoop R. Damodaran, Shishir Pandya, Josh C. Agar, Ye Cao, Rama K. Vasudevan, Ruijuan Xu, Sahar Saremi, Qian Li, Jieun Kim, Margaret R. McCarter, Liv R. Dedon, Tom Angsten, Nina Balke, Stephen Jesse, Mark Asta, Sergei V. Kalinin, and Lane W. Martin*

Leveraging competition between energetically degenerate states to achieve large field-driven responses is a hallmark of functional materials, but routes to such competition are limited. Here, a new route to such effects involving domain-structure competition is demonstrated, which arises from strain-induced spontaneous partitioning of PbTiO₃ thin films into nearly energetically degenerate, hierarchical domain architectures of coexisting c/a and a_1/a_2 domain structures. Using band-excitation piezoresponse force microscopy, this study manipulates and acoustically detects a facile interconversion of different ferroelastic variants via a two-step, three-state ferroelastic switching process (out-of-plane polarized $c^+ \rightarrow$ in-plane polarized $a \rightarrow$ out-of-plane polarized c^- state), which is concomitant with large nonvolatile electromechanical strains (≈1.25%) and tunability of the local piezoresponse and elastic modulus (>23%). It is further demonstrated that deterministic, nonvolatile writing/erasure of large-area patterns of this electromechanical response is possible, thus showing a new pathway to improved function and properties.

Large responses in ferroic systems tend to arise at chemically induced phase boundaries (i.e., morphotropic phase boundaries, MPBs) where interconversion of nearly energetically degenerate phases is possible. At such boundaries, application of the appropriate stimulus (i.e., electric field, stress, etc.) allows one to control the constituent phase fractions thereby providing a route to colossal physical responses.[1–3] Such effects are present in PbZr₁₋ₓTiₓO₃ ($x = 0.48$),[1] (1−x)PbMg₁/₃Nb₂/₃O₃-(x)PbTiO₃ (PMN-PT) ($x = 0.33$),[4] rare-earth doped BiFeO₃,[5–8] and other systems.[9–11] There are, however, only a limited number of systems that possess such boundaries and, therefore, alternative routes to generate such

structural competition with potential for large field-driven effects are desirable.

It has also been shown that even chemically simple materials, such as PbTiO₃, can be driven to phase competition under nonambient pressures and temperature.[12] In a similar vein, modern strain-engineering routes,[13–15] which have been extensively used to control ferroelectric order[16,17] and manipulate ferroelectric domain structures,[18–21] emerge as a promising route to induce structural instabilities and phase competition in simple, single-component ferroelectrics. In BiFeO₃, for example, strain was shown to drive the coexistence of tetragonal- and rhombohedral-like phases and corresponding large electromechanical strains (4–5%).[22,23] The observation of a strain-induced, MPB-like feature in BiFeO₃ provided a potential route to circumvent the limitations on susceptibilities in epitaxially constrained ferroelectric films.[24] Despite extensive interest, however, such strain-induced effects have not been found to be pervasive in materials and, thus, it is desirable to explore alternate strain-based pathways to generate structural competition with potential for large field-driven effects.

Here, we report a novel strain-induced domain-structure instability and competition in single-phase PbTiO₃ films where domain structure reconfiguration under external perturbation provides a route to large electromechanical responses. Through a combination of epitaxial thin-film growth, structural characterization, band-excitation piezoresponse spectroscopy

Dr. A. R. Damodaran, S. Pandya, Dr. J. C. Agar, R. Xu,
S. Saremi, J. Kim, L. R. Dedon, T. Angsten, Prof. M. Asta,
Prof. L. W. Martin
Department of Materials Science & Engineering
University of California
Berkeley, CA 94720, USA
E-mail: lwmartin@berkeley.edu
Dr. Y. Cao, Dr. R. K. Vasudevan, Dr. Q. Li, Dr. N. Balke,
Dr. S. Jesse, Dr. S. V. Kalinin
Center for Nanophase Materials Sciences
Oak Ridge National Laboratory
Oak Ridge, TN 37831, USA

Dr. R. K. Vasudevan, Dr. N. Balke, Dr. S. Jesse, Dr. S. V. Kalinin
Institute for Functional Imaging of Materials
Oak Ridge National Laboratory
Oak Ridge, TN 37831, USA
M. R. McCarter
Department of Physics
University of California
Berkeley, CA 94720, USA
Prof. L. W. Martin
Materials Sciences Division
Lawrence Berkeley National Laboratory
Berkeley, CA 94720, USA

ADVANCED
SCIENCE NEWS
www.advancedsciencenews.com

ADVANCED
MATERIALS
www.advmat.de

(BEPS) with acoustic detection, and phase-field modeling, we demonstrate a strain-regime (≈0.2–0.8%) wherein strain accommodation occurs by the formation of hierarchical domain architectures of coexisting c/a and a_1/a_2 domain structures. In this regime, the c/a and a_1/a_2 domain structures possess nearly degenerate energies and the two domain structures are individually unstable. This instability results in a spontaneous strain partitioning (akin to a strain-induced spinodal instability[25]) into a complex mixture of c/a and a_1/a_2 domain structures. This combination of features allows for facile interconversion among different ferroelastic variants resulting in a two-step, three-state switching process (out-of-plane polarized $c^+ \rightarrow$ in-plane polarized $a \rightarrow$ out-of-plane polarized c^- state). Leveraging this capability to interconvert between in- and out-of-plane polarized states, we demonstrate deterministic writing and erasure of ferroelastic domain structures with large out-of-plane electromechanical strains (≈1.25%), large changes in local piezoresponse, and variations in elastic modulus (>23%).

Analytical phenomenological and phase-field models have been used to predict the strain and field evolution of domain structures in numerous ferroelectrics.[26–30] In PbTiO$_3$ specifically, a systematic evolution from monodomain and out-of-plane polarized c domains at large compressive strains, to polydomain c/a domain structures (consisting of alternating c domains and in-plane polarized a domains) at small compressive or tensile strains, and finally to completely in-plane polarized a_1/a_2 domains at large tensile strains has been predicted and observed (**Figure 1**a).[31–33] Beyond these structures, phase-field models have suggested a complex domain structure coexistence near the c/a–a_1/a_2 boundary.[28] Such potential domain-structure coexistence is reminiscent of phase competition, and thus, could provide a route to large field-driven effects. To explore this concept, we employed pulsed-laser deposition (Experimental Section) to grow 40 nm thick PbTiO$_3$ films on SrTiO$_3$ (001), DyScO$_3$ (110), GdScO$_3$ (110), and SmScO$_3$ (110) substrates corresponding to lattice misfit strains of −1.3%, −0.2%, 0.3%, and 0.7%, respectively (note that all values are relative to the pseudocubic lattice parameter of PbTiO$_3$; dashed lines, Figure 1a). Following growth, detailed X-ray diffraction (XRD) studies (Figure S1 and S2, Supporting Information),
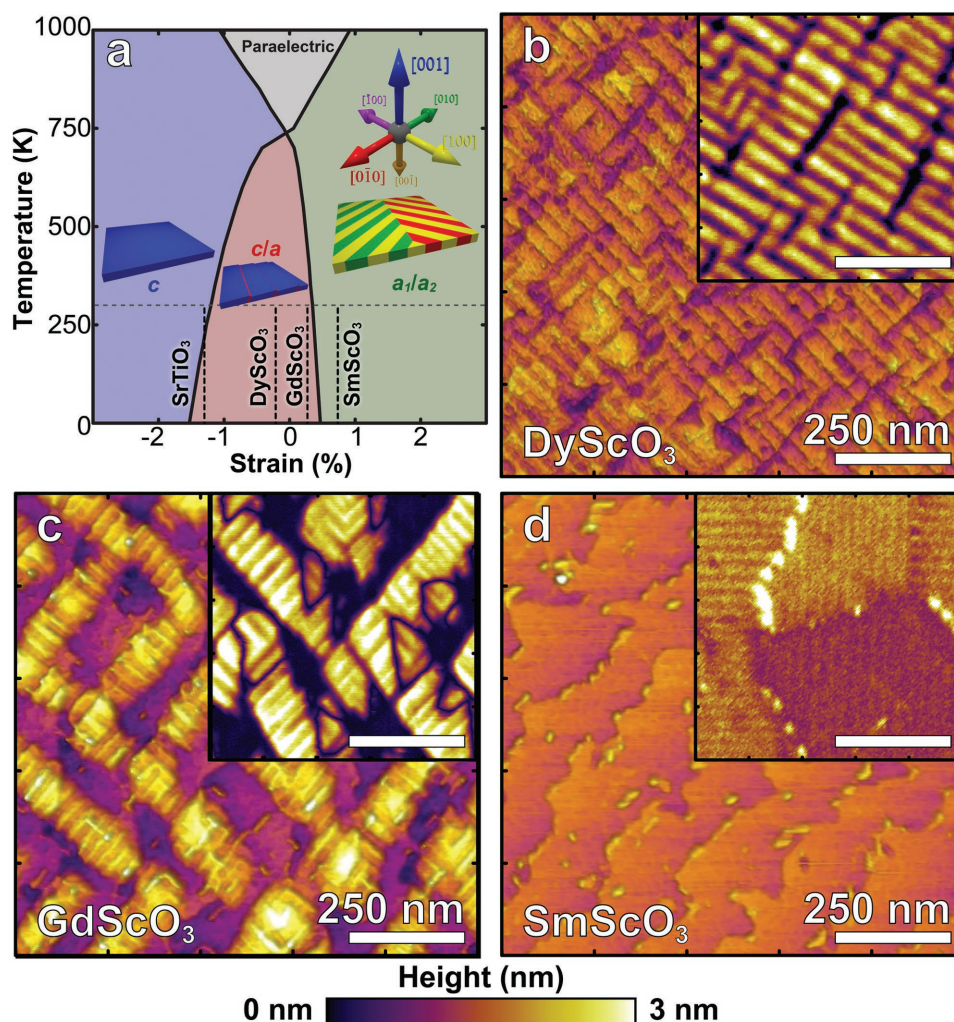

Figure 1. a) Analytical phenomenological modeling-based temperature–strain phase diagram revealing the stability regimes for c, c/a, and a_1/a_2 domain structures. Strain positions for the substrates used are shown as dashed lines in (a). b–d) Topography and out-of-plane piezoresponse amplitude (inset) of PbTiO$_3$ films grown on DyScO$_3$ (b), GdScO$_3$ (c), and SmScO$_3$ (d) substrates.

and scanning-probe-based studies of topography (Figure 1b–d) and piezoresponse force microscopy (PFM, vertical amplitude, inset Figure 1b–d; both vertical and lateral amplitude and phase images are provided; Figure S3, Supporting Information) were conducted. In all cases the films were found to be single-phase, but the surface topography and the corresponding domain structures were dramatically different. Consistent with expectations of analytical phenomenological models, the topography and domain structure of the $PbTiO_3/SrTiO_3$ (Figure S3, Supporting Information) and $PbTiO_3/DyScO_3$ (Figure 1b) heterostructures reveal predominantly c and c/a domain structures, respectively, wherein the a domain fraction increases with decreasing compressive strain. Similar studies of $PbTiO_3/GdScO_3$ heterostructures (Figure 1c), however, reveal the emergence of a complex hierarchical domain architecture consisting of a mixture of c/a and a_1/a_2 domain structures that is not predicted in analytical phenomenological models. Further increasing the tensile strain, the $PbTiO_3/SmScO_3$ heterostructures (Figure 1d) show an a_1/a_2 domain structure which has a small fraction of c/a domains indicating its nearness to the phase boundary between the hierarchical regime and the regime of a_1/a_2 domain structure (inset, Figure 1d).

Further analysis of the topography (**Figure 2**a) and PFM (Figure 2b,c) studies of the $PbTiO_3/GdScO_3$ heterostructures reveal the nature of the hierarchical domain architecture. Two distinct regions are observed. First, the regions with elevated,

saw-tooth-like topography and domain walls along the $\langle 100 \rangle_{pc}$ (schematic inset, Figure 2b) are found to be a type of distorted c/a domain structure. A line trace across this band (inset, Figure 2a) reveals that the c and a domains are tilted by $\approx 1.17°$ and $\approx 0.75°$ relative to the substrate surface, respectively. The second region, corresponding to the recessed, flat topography, exhibits reduced out-of-plane and enhanced in-plane piezoresponse with 90° domain walls along the $\langle 110 \rangle_{pc}$ (Figure 2c); typical of a_1/a_2 domain structures (schematic inset, Figure 2c). Further insights into the various components of the hierarchical domain architectures can be obtained by comparing features in the nanoscale topography and piezoresponse images with 3D, synchrotron-based reciprocal space mapping (RSM) studies. An RSM about the 110-diffraction condition of the $GdScO_3$ substrate (Figure 2d) reveals film peaks corresponding to $00l$-oriented c domains (out-of-plane lattice parameter of 4.104 Å, crystallographic tilt of 1.17°), and two versions of in-plane polarized a domains: (1) an untilted variant (corresponding to the classic a_1/a_2 structure, with out-of-plane lattice parameter of 3.926 Å) and (2) a tilted variant (corresponding to the a domains in the c/a structure with an out-of-plane lattice parameter of 3.911 Å and a crystallographic tilt of 0.65°). These tilt angles match well with the scanning-probe-based measurements for the different regions (inset, Figure 2a). Additionally, the large difference in the out-of-plane lattice parameters of the a domains within the c/a and the a_1/a_2 domain structures is
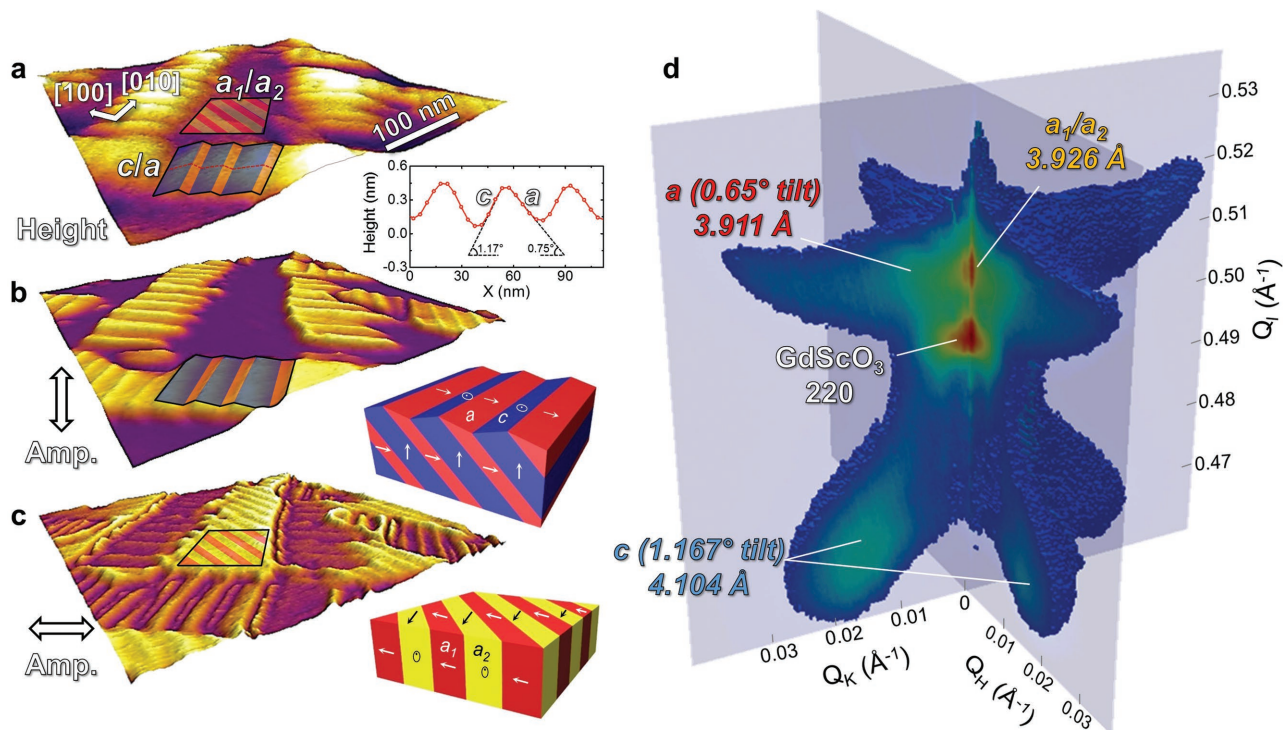

Figure 2. a) 3D representation of the topography of $PbTiO_3$ hierarchical domain architectures grown on $GdScO_3$ (110). Inset shows line trace (red-dashed line) indicating the topography and crystallographic tilts. b) Vertical PFM (amplitude) response superimposed on 3D representation of the topography of the hierarchical $PbTiO_3$ domain structure. Inset shows a schematic representation of the domain structure within a c/a region as indicated by the shaded box. c) Lateral PFM (amplitude) response superimposed on 3D representation of the topography of the hierarchical $PbTiO_3$ domain structure. Inset shows a schematic representation of the domain structure within an a_1/a_2 region as indicated by the shaded box. d) 3D, synchrotron-based RSM about the 110-diffraction peak of the $GdScO_3$ substrate (capturing 001-diffraction peaks of the $PbTiO_3$) indicating the extracted lattice parameters and crystallographic tilts.
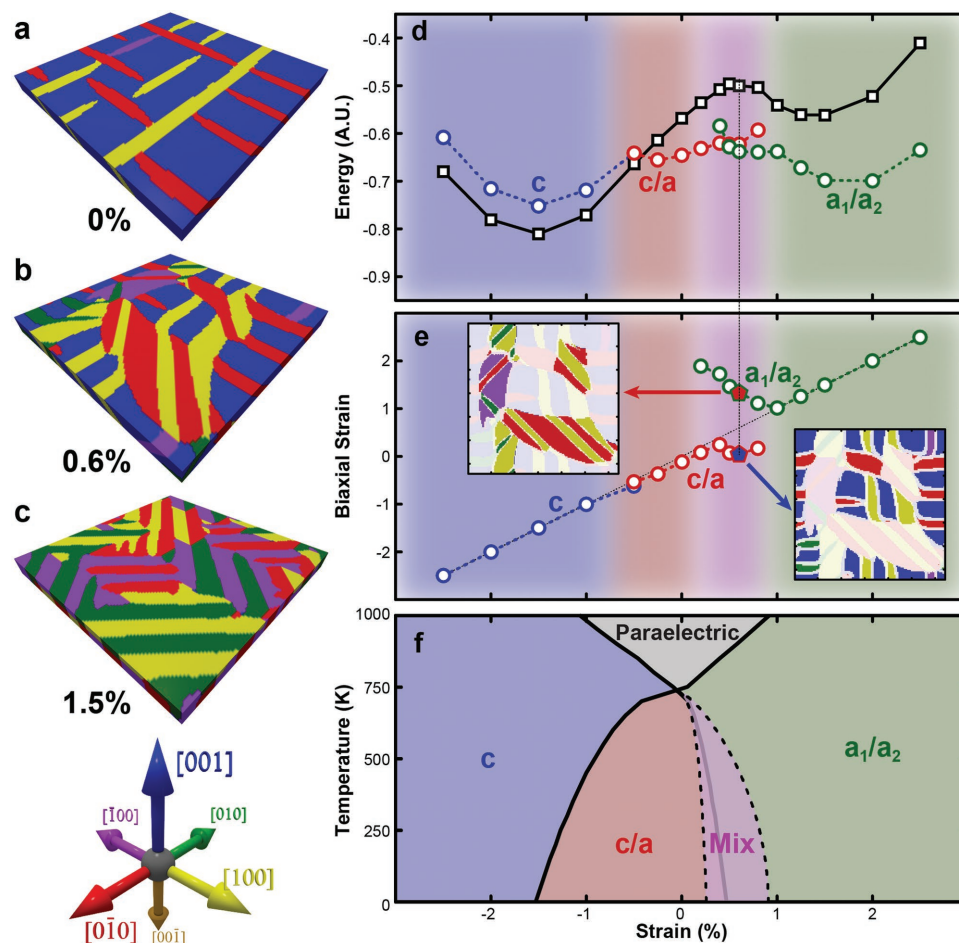
**ADVANCED
SCIENCE NEWS**

www.advancedsciencenews.com

**ADVANCED
MATERIALS**

www.advmat.de

Figure 3. Phase-field predicted stable domain configurations showing: a) c/a domain structure (0% strain), b) c/a and a_1/a_2 hierarchical domain architectures (0.6% strain), and c) a_1/a_2 domain structure (1.5% strain). d) Corresponding strain-energy landscape (square points, black, solid curve) and the sum of Landau and elastic energy density within the constituent domain structure (circles, dashed line) including: c (blue circles), c/a (red circles), and a_1/a_2 (green circles). e) Strain accommodation in the different domain structures such that within the region of negative curvature (violet regions, for example at 0.6% strain as shown here), the material partitions itself into two domains structures: c/a domains at a strain of 0.1% (right inset) and a_1/a_2 domains at a strain of 1.35% strain (left inset). f) The resulting temperature–strain phase diagram showing the region of hierarchical domain structure between c/a and a_1/a_2 regions as an adaptation of classic phase diagrams for this system.

indicative of a complex strain accommodation in these hierarchical domain architectures.

To understand the energetics and the nature of strain distribution in the hierarchical domain architectures, and to illuminate the mechanism behind the formation of this complex structure, we employed phase-field models (Experimental Section). In our models, we focused on the strain range from −2.5 to 2.5% and on obtaining the lowest-energy structure (Figure S4, Supporting Information). We observe that the domain structure evolves from monodomain c ($\lesssim$−1%) to c/a ($\approx$−0.5 to 0%, **Figure 3**a) with decreasing compressive strain. Moving to tensile strain, at small values we note the nucleation of a_1/a_2 domain structures; corresponding to the emergence of the hierarchical domain architectures ($\approx$0.2–0.8%, Figure 3b). Further increasing the tensile strain causes an increase in the fraction of a_1/a_2 domain structures within hierarchical domain architecture until eventually transforming into a classical a_1/a_2 domain structure ($\gtrsim$1%, Figure 3c). The overall lowest strain-energy landscape (black line, Figure 3d) is

characterized by the presence of two local minima separated by a region of negative curvature (akin to a strain-induced spinodal instability[25,34,35]). We note that the hierarchical domain architectures are observed within this region of negative curvature and this region corresponds to a strain-energy landscape which is nearly degenerate. This is obvious when one probes how the domain structure fractions (Figure S5, Supporting Information) and various energies of the system (i.e., Landau, elastic, gradient, and electrostatic; Figure S6, Supporting Information) evolve with misfit strain. While the electrical and gradient energies increase monotonically with increasing tensile strain, the dominant energies are found to be the elastic and Landau components and thus we focus our attention on the sum of these two energies within each constituent domain structure (multicolor line, Figure 3d). These energies combine to drive the formation of the two local minima corresponding to monodomain c (−2.5 to −1%, blue circles, Figure 3d) and the a_1/a_2 (1.0–2.5%, green circles, Figure 3d) domain structures. With decreasing compressive strain (−0.5 to 0.2%), a domains form in the c

ADVANCED
SCIENCE NEWS
www.advancedsciencenews.com

ADVANCED
MATERIALS
www.advmat.de

matrix, reducing the combined elastic and Landau energies (red circles, Figure 3d) and producing a classic c/a domain structure (Figure 3a). In the regime where hierarchical domain architectures are observed, we note that the combined elastic and Landau energies for both the c/a and a_1/a_2 domain structures are nearly equivalent; hence they coexist (violet region, Figure 3d). This coexistence, in turn, is found to be formed by a decomposition of the material into two domain structures which effectively partitions the average biaxial strain by forming the appropriate mixture of c/a domains (which stay clamped to an in-plane strain of ≈0.1%) and a_1/a_2 domains (which exhibit strains between 1–2% with increasing tensile strain) such that the overall strain balances to the value set by the substrate (≈0.2–0.8%, Figure 3e). For instance, the hierarchical domain architecture observed at a misfit strain of 0.6% results from a partitioning of the material into c/a and a_1/a_2 domain structures with an in-plane strain of ≈0.1% and ≈1.35%, respectively (inset, Figure 3e). In this regime, any change in epitaxial strain or, by extension, any external perturbation (e.g., electric field, temperature, stress) can be accommodated by changing the relative c/a and a_1/a_2 domain fractions while keeping the total energy essentially unchanged. Said another way, by constraining the material with the appropriate biaxial strain conditions, it is possible to produce structural competition between different domain structures (analogous to phase competition in MPB systems) in single-phase PbTiO$_3$. In fact, the current system exhibits several features characteristic of MPB systems, including: energetic degeneracy of coexisting structures,

reduced structural and polarization anisotropy,[3,36] and low domain-wall-formation energies[37] in the hierarchical domain architectures (Figure S7, Supporting Information). Finally, to further distinguish this regime of hierarchical domain architectures from the traditionally observed domain structures, we have used additional temperature-dependent phase-field studies (Figure S8, Supporting Information) to approximate this region and provide a revised temperature–strain phase diagram (Figure 3f).

The potential for electric-field driven response was explored via PFM-based BEPS[38,39] (Experimental Section and Figure S9 and S10, Supporting Information) which allows for the visualization of the switching process (Figure S11 and S12, Supporting Information). To conduct this experiment, we applied a bipolar triangular switching waveform using a scanning-probe tip in a square-grid (3 µm spacing between points) and measured the piezoresponse, phase, cantilever loss, and cantilever contact resonance (indicative of elastic modulus) at each voltage step (a total of four voltage cycles are completed at each point; data in **Figure 4** is from the 4th cycle, but the data from the 2nd and 3rd cycles look similar). Prior to, and following switching, PFM and topography scans were obtained and image registry techniques were employed to observe any structural changes. From this analysis, two characteristic switching processes were observed; each of which revealed a high degree of correlation to the initial domain structure. First, switching in a purely c/a region (Figure 4a) reveals piezoresponse loops with a sharp, single positive and negative coercive bias,
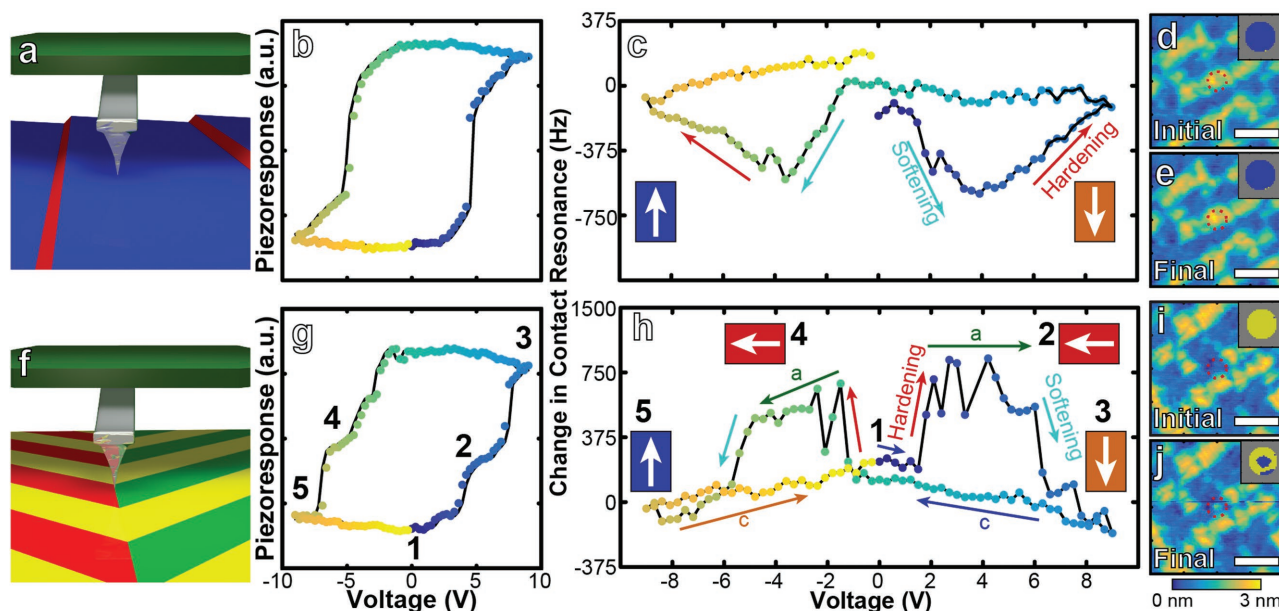

Figure 4. Band excitation piezoresponse spectroscopy (BEPS) studies on 80 nm PbTiO$_3$/BaSr$_{0.5}$Ru$_{0.5}$O$_3$/GdScO$_3$ heterostructures with coexisting hierarchical c/a and a_1/a_2 domain architectures. a,b) Schematic illustration of a c/a region (a), and corresponding out-of-plane piezoresponse hysteresis loop (b) obtained from such a region. c) Contact resonance frequency loops with various polarization states through the switching process indicated. d,e) Topographic images of the region prior to (d) and following (e) switching revealing an unchanged domain structure. Inset shows a binary image of the 75 nm region directly under the PFM tip. f–g) Schematic illustration of an a_1/a_2 region (f), and corresponding out-of-plane piezoresponse hysteresis loop (g) and contact resonance frequency loop (h) taken in such a region revealing a three-state ferroelastic switching process (c^+, a, and c^-) with high (low) piezoresponse and low (high) contact resonance states characteristic of c (a) domains. Throughout the switching process the polarization states are indicated. i,j) Topographic images of the region prior to (i) and following (j) switching revealing the nucleation of a c domain within an a_1/a_2 domain structure. Inset shows a binary image of the 75 nm region directly under the PFM tip. Scale bars in all images are 500 nm.

**ADVANCED
SCIENCE NEWS**

www.advancedsciencenews.com

**ADVANCED
MATERIALS**

www.advmat.de

consistent with ferroelectric switching for an out-of-plane polarized, tetragonal ferroelectric (Figure 4b; Figure S11, Supporting Information). The voltage-contact resonance frequency loops (Figure 4c), again indicative of the elastic modulus of the film, reveal a butterfly loop shape with softening of the lattice during the switching, and hardening during saturation, consistent with prior reports.[40–43] Specifically, as positive bias is applied, there is a rapid change in the piezoresponse as the film switches, resulting in elastic softening up to a bias of ≈4 V. Further increasing the voltage gives rise to saturation of the piezoresponse and, correspondingly, elastic hardening, indicating that the structure has fully reoriented under the applied field. As the bias is decreased towards 0 V, the resonance frequency remains essentially constant until, under negative bias, an identical switching process in the opposite direction is observed. Looking at the initial and final topographic images (Figure 4d,e, respectively) we note no change in the topography and domain structures.

Focusing now on to the second type of switching, occurring when applying a bias in an a_1/a_2 domain region (Figure 4f; additional loops are provided in Figure S12, Supporting Information), an atypical switching process is observed. The piezoresponse hysteresis loops exhibit intermediate stable states with a reduced piezoresponse (labeled 2 and 4, Figure 4g) relative to the saturation states (labeled 5 and 3, Figure 4g). Corresponding analysis of the voltage-contact resonance loops (Figure 4h), reveals an unconventional response wherein an initial elastic hardening to a stiffer intermediate state is observed (we note that this type of response persists through multiple switching cycles). In particular, upon increasing the bias, there is a rapid and abrupt increase in the contact resonance, indicative of a transition to a mechanically stiffer state (1→2, Figure 4h), which corresponds to the intermediate, low piezoresponse state (2, Figure 4g). Considering the anisotropy in stiffness ($C_{11} \approx 105$ GPa, $C_{33} \approx 230$ GPa) and piezoelectric coefficients ($d_{33} \approx 83.7$ pm V^{-1}, $d_{11} \approx 0$ pm V^{-1}) in tetragonal PbTiO$_3$,[44] the transition observed corresponds to a 90° ferroelastic switching from up-polarized c to in-plane polarized a. To validate this observation, contact resonance measurements (without bias) in purely c and a domain regions were completed and reveal an increase in the contact resonance frequency of ≈2000 Hz from c to a (Figure S13, Supporting Information). Thus, this increase in elastic modulus represents the direct detection of 90° ferroelastic switching from an up-polarized c^+ to in-plane polarized a. Continuing to increase the positive bias results in an abrupt reduction of the contact resonance indicative of a transition to a mechanically softer state (2→3, Figure 4h) which corresponds with the saturation of the piezoresponse (3, Figure 4g). This indicates a second 90° ferroelastic switch from the in-plane polarized a to a down-polarized c^- domain. As the field is subsequently reduced, the region under the tip remains down-polarized c^-, until reaching the negative coercive field, wherein it undergoes a transition to in-plane polarized a as indicated by a rapid increase in the contact resonance (3→4, Figure 4h) and the intermediate state with low piezoresponse (4, Figure 4g). Upon further increasing the negative bias, the material transitions from the in-plane polarized a to an up-polarized c^+ as indicated by a rapid decrease in the contact resonance (4→5, Figure 4h) and saturation of the piezoresponse (5, Figure 4g).

Comparison of the initial (Figure 4i) and final (Figure 4j) topographic images reveals the nucleation of a stable c domain within the a_1/a_2 matrix. These studies illuminate the role of domain-structure competition in reducing clamping effects, which results in an acoustically detected two-step, three-state ferroelectric switching process, and facilitates the interconversion of ferroelastic domain structure variants.

Such facile electric-field-driven ferroelastic switching provides a promising route to controllably reconfigure domain architectures important for a range of applications. To demonstrate the potential of this system, we focus on a hierarchical domain architectures consisting almost entirely of a_1/a_2 domain structures (as found in films at $\varepsilon_s = 0.7\%$). As-grown, the films reveal a flat topography (height, **Figure 5**a) and a diminished out-of-plane piezoresponse (color scale, Figure 5a) corresponding to a_1/a_2 domain structures. A bias pattern (7 V) was applied using the PFM tip to ferroelastically write an array of out-of-plane polarized c domain lines which protrude from the surface (height, Figure 5b) and exhibit enhanced out-of-plane piezoresponse (color scale, Figure 5b). To erase these c domains, in-plane electric fields (≈100 kV cm^{-1}) were applied using interdigitated electrodes restoring the as-grown topography (height, Figure 5c) and out-of-plane piezoresponse (color scale, Figure 5c). Line traces across the switched regions (height, Figure 5a–c) reveal that the electric-field induced ferroelastic interconversion from a to c is accompanied by ≈0.5 nm changes in the surface topography; corresponding to large and recoverable out-of-plane electromechanical strains of ≈1.25%. The versatility of this effect is demonstrated by electrically writing an arbitrary pattern over a large area (resembling the Cal logo, Figure 5d). Such deterministic, reversible, and nonvolatile control of ferroelastic switching–in a clamped thin film no less–is promising to control the dielectric, optical, acoustic, etc., properties of materials at the nanoscale which has implications for a range of applications including nanoelectromechanical systems,[45] reconfigurable metamaterials,[46,47] piezotronics,[48] smart/adaptable surfaces and modules,[49,50] and much more. For example, in addition to the large changes in topography and piezoresponse, the inherent anisotropy in PbTiO$_3$ means that these same ferroelastic interconversions give rise to a reversible ≈23% change in the local Young's modulus of the material (Figure S13 and S14, Supporting Information). Such effects point to a rich potential for exotic nanoscale design of materials and mesostructures.

In summary, a strain-based pathway to induce domain-structure competition in PbTiO$_3$ has been demonstrated to result in field-induced ferroelastic interconversions that give rise to large responses. Such effects are made possible by the nearly energetically degenerate, hierarchical domain architectures of coexisting c/a and a_1/a_2 domain structures which drives an acoustically detectable two-step, three-state ferroelastic switching process. This allows for deterministic writing and erasure of ferroelastic domain-structure variants with large out-of-plane electromechanical strains (≈1.25%) and tunability of the local piezoresponse and elastic modulus (>23%). Such structures, in turn, are useful for deterministic control of nanoscale modulations in thermal, electrical, mechanical, and optical susceptibilities and motivate the exploration of other systems wherein similar approaches can be used to induce
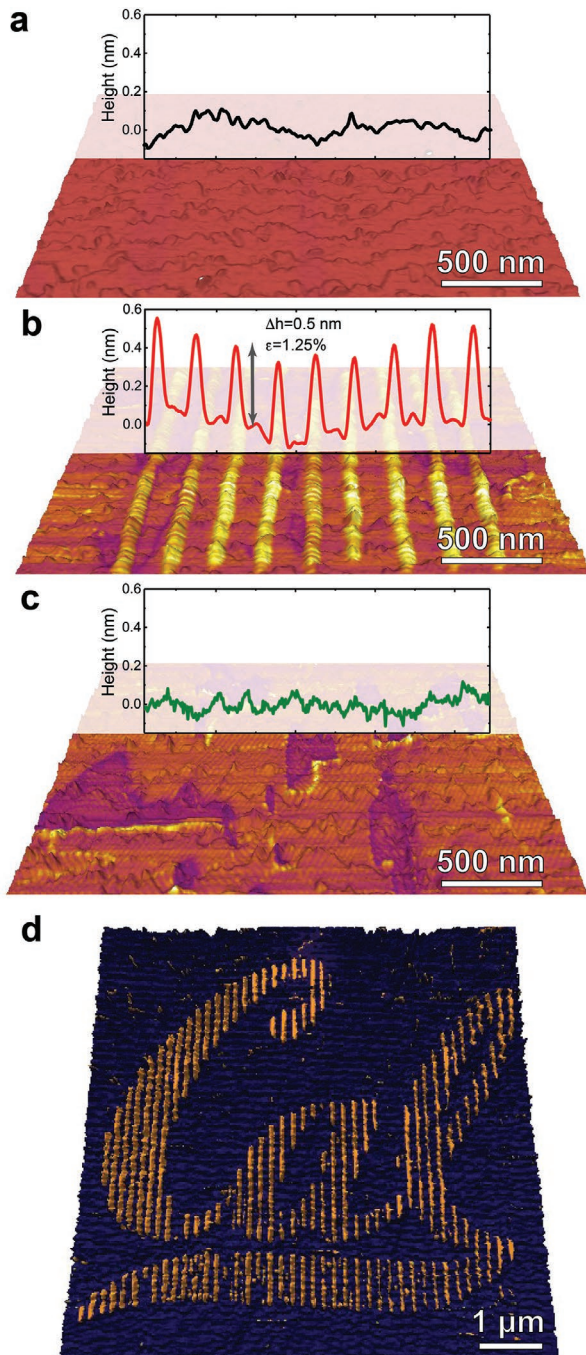
Figure 5. Superimposed topography and vertical PFM (amplitude) response for a 40 nm thick $PbTiO_3$ film grown with $\varepsilon_s = 0.7\%$ with predominantly a_1/a_2 structure. a) Shows the initial a_1/a_2 domain structure and an atomically terraced surface (as indicated by the line trace in height). b) Reveals a deterministically written pattern of c/a domains within the a_1/a_2 region wherein large surface displacements are observed (line trace in height shows ≈0.5 changes). c) Shows that such structures can be erased by application of an in-plane electric field, restoring the surface to the original smooth state (line trace in height). The inset height line traces reveal the evolution of the surface topography and indicate the potential for reversible electromechanical strains of 1.25%. d) Electrically written ferroelastic pattern (Cal logo) on a 10 μm² as-grown. The Cal logo, which is a registered trademark and intellectual property of the Regents of the University of California, is reproduced with permission.

hierarchical ferroelastic domain architectures capable of exhibiting new functionalities and improved performance.

Experimental Section

Film Growth and Samples: Single-layer $PbTiO_3$ thin films were synthesized via pulsed-laser deposition using a KrF excimer laser (248 nm, LPX 300, Coherent), in an on-axis geometry with a 60 mm target-to-substrate spacing. Films were grown on $SrTiO_3$ (001), $DyScO_3$ (110), $GdScO_3$ (110), and $SmScO_3$ (110) substrates which were affixed to the heater using Ag-paint and subsequently heated to the deposition temperature of 675 °C in a dynamic oxygen pressure of 200 mTorr. 40 nm thick $PbTiO_3$ thin films were grown on these substrates by ablating $PbTiO_3$ targets (Praxair) at a laser fluence of 1.8 J cm⁻², and a laser repetition rate of 15 Hz. The BEPS studies were conducted on 80 nm thick $PbTiO_3$ films that were grown on 20 nm thick $Ba_{0.5}Sr_{0.5}RuO_3$-buffered $SmScO_3$ (110) substrates. The $Ba_{0.5}Sr_{0.5}RuO_3$ bottom electrode layer was grown on $SmScO_3$ (110) substrates at a heater temperature of 750 °C in a dynamic oxygen pressure of 20 mTorr by ablating a $Ba_{0.5}Sr_{0.5}RuO_3$ target (Praxair) at a laser fluence of 1.8 J cm⁻² and a laser repetition rate of 2 Hz. Following growth, all heterostructures were cooled to room temperature in a static oxygen pressure of 760 Torr at 5 °C min⁻¹.

Structural Characterization—Laboratory-Based X-Ray Diffraction: Wide-angle θ–2θ X-ray diffraction patterns and symmetric reciprocal space maps were obtained with a Panalytical X'Pert Pro XRD machine with a Cu source.

Structural Characterization—Synchrotron X-Ray diffraction: 3D reciprocal space maps providing additional insights into the structure of hierarchical domain architectures observed in the $PbTiO_3/GdScO_3$ (110) heterostructures were obtained at the Sector 33-BM-C beamline of the Advanced Photon Source, Argonne National Laboratory. In order to obtain a highly monochromatic beam with negligible higher-order harmonics, a double crystal monochromator in conjunction with two mirrors was used. Moreover, excellent accuracy of a Huber 4-circle diffractometer in combination with a PILATUS 100K pixel detector allowed to determine the orientation of the crystal reliably and obtain the scans with high accuracy. The X-ray wavelength used for these measurements was 0.8 Å (15.5 keV).

Topography and Domain Structure Characterization: Study of the $PbTiO_3$ thin films was carried out using atomic force microscope (AFM) (MFP-3D, Asylum Research). Dual AC Resonance Tracking piezoresponse force microscopy was used to image the domain structure.

Phase-Field Studies for Domain Structure Evolution: In the phase-field modeling of the single layer $PbTiO_3$ thin films, the evolution of the polarization was obtained by solving the time-dependent Landau–Ginzburg–Devonshire equations

$$\frac{\partial P_i(x,t)}{\partial t} = -L \frac{\delta F}{\delta P_i(x,t)}, \, i = 1, 2, 3 \tag{1}$$

where P_i is the polarization vector, x and t are position the time, and L is the kinetic coefficient related to the domain wall mobility. The contributions to the total free energy F include the Landau bulk energy, elastic energy, electric (electrostatic) energy, and gradient energy, i.e.

$$F = \int \left(f_{Landau} + f_{Elastic} + f_{Electric} + f_{Gradient} \right) dV \tag{2}$$

Detailed expressions for each of the energy density contributions, and the material constants for $PbTiO_3$ used in the simulations were collected from the literature and these include the Landau potentials, elastic constants, electrostrictive coefficients, background dielectric constants, and gradient energy coefficients.[28,51–56]

3D phase-field simulations of $PbTiO_3$ was done using a realistic 3D geometry sampled on a fine grid mesh of $(128\Delta x_1) \times (128\Delta x_2) \times (32\Delta x_3)$ with $\Delta x_1 = \Delta x_2 = \Delta x_3 = 1$ nm. The thickness of the substrate, film, and

**ADVANCED
SCIENCE NEWS**

www.advancedsciencenews.com

**ADVANCED
MATERIALS**

www.advmat.de

air are ($10\Delta x_3$), ($20\Delta x_3$), and ($2\Delta x_3$), respectively. Periodic boundary conditions were applied in the in-plane direction (x_1 and x_2) while the thin film was simulated by properly choosing the mechanical and electrical boundary condition along the out-of-plane direction (x_3). Random noise was used as the initial setup to simulate the thermal fluctuation during the annealing process. This was employed to obtain equilibrium room-temperature domain structures for an extensive range of misfit strain values from −2.5% to 2.5%. Each of these structures stabilized from random noise was then subjected to a subsequent set of simulations in which their initial misfit strain was systematically varied from −2.5% to 2.5% to obtain a new set of final equilibrium states. This methodology yielded a number of different structures for each value of misfit strain. Subsequent analysis was conducted on domain configurations possessing the lowest energy for each value of misfit strains.

Band-Excitation Piezoresponse Spectroscopy: Studies were performed at the Center for Nanophase Materials Science at Oak Ridge National Laboratory using a custom Cypher microscope (Asylum Research) controlled with a Labview- and Matlab-based band-excitation controller. A bipolar triangular switching waveform was applied using a scanning-probe tip in a square-grid (3 µm spacing between points) and measured the piezoresponse, phase, cantilever loss, and cantilever contact resonance at each voltage step. The use of band excitation for these measurements was crucial as it minimized effects from changing tip–sample contact resonances that can alter the observed response, enabling the measurement of piezoresponse to be consistent throughout multiple dimensions (i.e., frequency, spatial, voltage, time, and so on; Figure S9 and S10, Supporting Information). All measurements were carried out using Pt/Ir-coated probe tip (NanoSensor PPP-EFM). BEPS measurements were measured at a resonance frequency of ≈330 kHz (with a BE bandwidth of 60 kHz). The DC voltage was chosen such that the piezoelectric hysteresis loops were saturated in both the positive and negative direction. The local piezoresponse was measured at remanence (following a dwell time of 0.5 ms) with a BE waveform of sinc character with a Vpp of 1 V. Unlike conventional PFM techniques which measure the local piezoresponse with a scanning probe at a single or dual frequencies near the cantilever resonance, BEPS measures piezoresponse using a frequency band near the cantilever resonance, enabling direct measurement of the full cantilever resonance characteristics.

Photothermal Excitation Contact Rresonance AFM Measurements: These measurements were employed to obtain contact resonance maps for $PbTiO_3$ thin films with hierarchical domain architectures, providing an estimate of elastic modulus differences between the *c*- and *a*-oriented domains. These studies were conducted at the Center for Nanophase Materials Science at Oak Ridge National Laboratory and were performed under ambient environment on a commercial AFM (Cypher, Asylum Research) equipped with a BlueDrive photothermal excitation module. Pt/Ir-coated conductive Si probes, Nanosensor PPP-EFM, were used, which typically have a moderate stiffness of 4–5 N m^{-1} and resonance frequency of 75–80 kHz as experimentally found. The set point force was maintained at ≈350 nN for all contact-mode measurements. Typically, 1–5 mW BlueDrive laser power was used to excite the cantilevers leading to a dynamic indentation force of a few tens' nN. The contact resonance frequency shifts as a function of the local elastic stiffness of samples and as such is captured in the image/spectrum data.

Supporting Information

Supporting Information is available from the Wiley Online Library or from the author.

Acknowledgements

Conflict of Interest

The authors declare no conflict of interest.

Keywords

[1] B. Jaffe, W. R. Cook, H. Jaffe, in *Piezoelectric Ceramics* (Eds: B. Jaffe, W. R. Cook, H. Jaffe), Elsevier, London, UK **1971**, p. 321.

[2] B. Noheda, D. E. Cox, *Phase Transitions* **2006**, *79*, 5.

[3] Y. Jin, Y. Wang, A. Khachaturyan, J. Li, D. Viehland, *J. Appl. Phys.* **2003**, *94*, 3629.

[4] S. Choi, T. Shrout, S. Jang, A. Bhalla, *Ferroelectrics* **1989**, *100*, 29.

[5] S. Fujino, M. Murakami, A. Varatharajan, S.-H. Lim, V. Nagarajan, C. J. Fennie, M. Wuttig, L. Salamanca-Riba, I. Takeuchi, *Appl. Phys. Lett.* **2008**, *92*, 202904.

[6] C.-J. Cheng, D. Kan, S.-H. Lim, W. R. McKenzie, P. R. Munroe, L. G. Salamanca-Riba, R. L. Withers, I. Takeuchi, V. Nagarajan, *Nano Lett.* **2009**, *80*, 014109.

[7] D. Kan, L. Pálová, V. Anbusathaiah, C. J. Cheng, S. Fujino, V. Nagarajan, K. M. Rabe, I. Takeuchi, *Adv. Funct. Mater.* **2010**, *20*, 1108.

[8] J. Walker, H. Simons, D. O. Alikin, A. P. Turygin, V. Y. Shur, A. L. Kholkin, H. Ursic, A. Bencan, B. Malic, V. Nagarajan, T. Rojac, *Sci. Rep.* **2016**, *6*, 19630.

[9] E. Cross, *Nature* **2004**, *432*, 24.

[10] Y. Saito, H. Takao, T. Tani, T. Nonoyama, K. Takatori, T. Homma, T. Nagaya, M. Nakamura, *Nature* **2004**, *432*, 84.

[11] J. Rödel, W. Jo, K. T. P. Seifert, E.-M. Anton, T. Granzow, D. Damjanovic, *J. Am. Ceram. Soc.* **2009**, *92*, 1153.

[12] M. Ahart, M. Somayazulu, R. E. Cohen, P. Ganesh, P. Dera, H. Mao, R. J. Hemley, Y. Ren, P. Liermann, Z. Wu, *Nature* **2008**, *451*, 545.

[13] L. W. Martin, A. M. Rappe, *Nat. Rev. Mater.* **2016**, *2*, 16087.

[14] A. R. Damodaran, J. C. Agar, S. Pandya, Z. Chen, L. Dedon, R. Xu, B. Apgar, S. Saremi, L. W Martin, *J. Phys.: Condens. Matter* **2006**, *28*, 263001.

[15] D. G. Schlom, L.-Q. Chen, C. J. Fennie, V. Gopalan, D. A. Muller, X. Pan, R. Ramesh, R. Uecker, *MRS Bull.* **2014**, *39*, 118.

[16] J. H. Haeni, P. Irvin, W. Chang, R. Uecker, P. Reiche, Y. L. Li, S. Choudhury, W. Tian, M. E. Hawley, B. Craigo, A. K. Tagantsev, X. Q. Pan, S. K. Streiffer, L. Q. Chen, S. W. Kirchoefer, J. Levy, D. G. Schlom, *Nature* **2004**, *430*, 758.

[17] K. J. Choi, M. Biegalski, Y. L. Li, A. Sharan, J. Schubert, R. Uecker, P. Reiche, Y. B. Chen, X. Q. Pan, V. Gopalan, L.-Q. Chen, D. G. Schlom, C. B. Eom, *Science* **2004**, *306*, 1005.

[18] Y.-H. Chu, Q. Zhan, L. W. Martin, M. P. Cruz, P.-L. Yang, G. W. Pabst, F. Zavaliche, S.-Y. Yang, J.-X. Zhang, L.-Q. Chen, D. G. Schlom, I.-N. Lin, T.-B. Wu, R. Ramesh, *Adv. Mater.* **2006**, *18*, 2307.

[19] J. Karthik, A. Damodaran, L. W. Martin, *Phys. Rev. Lett.* **2012**, *108*, 16760.

[20] R. Xu, J. Zhang, Z. Chen, L. W. Martin, *Phys. Rev. B.* **2015**, *91*, 144106.

[21] J. C. Agar, A. R. Damodaran, M. B. Okatan, J. Kacher, C. Gammer, R. K. Vasudevan, S. Pandya, L. R. Dedon, R. V. K. Mangalam, G. A. Velarde, S. Jesse, N. Balke, A. M. Minor, S. V. Kalinin, L. W. Martin, *Nat. Mater.* **2016**, *15*, 549.

[22] R. J. Zeches, M. D. Rossell, J. X. Zhang, A. J. Hatt, Q. He, C.-H. Yang, A. Kumar, C. H. Wang, A. Melville, C. Adamo, G. Sheng, Y.-H. Chu, J. F. Ihlefeld, R. Erni, C. Ederer, V. Gopalan, L. Q. Chen, D. G. Schlom, N. A. Spaldin, L. W. Martin, R. Ramesh, *Science* **2009**, *326*, 977.

[23] A. R. Damodaran, C.-W. Liang, Q. He, C.-Y. Peng, L. Chang, Y.-H. Chu, L. W. Martin, *Adv. Mater.* **2011**, *23*, 3170.

[24] V. Nagarajan, S. Prasertchoung, T. Zhao, H. Zheng, J. Ouyang, R. Ramesh, *Appl. Phys. Lett.* **2004**, *84*, 5225.

[25] R. Bruinsma, A. Zangwill, *J. Phys.* **1986**, *47*, 2055.

[26] V. Koukhar, N. Pertsev, R. Waser, *Phys. Rev. B.* **2001**, *64*, 214103.

[27] Q. Y. Qiu, V. Nagarajan, S. P. Alpay, *Phys. Rev. B.* **2008**, *78*, 064117.

[28] Y. L. Li, S. Y. Hu, Z. K. Liu, L. Q. Chen, *Acta Mater.* **2002**, *50*, 395.

[29] L. Q. Chen, *J. Am. Ceram. Soc.* **2008**, *91*, 1835.

[30] J. X. Zhang, G. Sheng, L. Q. Chen, *Appl. Phys. Lett.* **2010**, *96*, 132901.

[31] J. Karthik, A. R. Damodaran, L. W. Martin, *Phys. Rev. Lett.* **2012**, *108*, 167601.

[32] L. Feigl, L. J. McGilly, N. Setter, *Ferroelectrics* **2014**, *465*, 36.

[33] S. Matzen, O. Nesterov, G. Rispens, J. A. Heuver, M. Biegalski, H. M. Christen, B. Noheda, *Nat. Commun.* **2014**, *5*, 4415.

[34] A. R. Damodaran, S. Lee, J. Karthik, S. MacLaren, L. W. Martin, *Phys. Rev. B.* **2012**, *85*, 024113.

[35] F. Xue, Y. Li, Y. Gu, J. Zhang, L. Q. Chen, *Phys. Rev. B.* **2016**, *94*, 220101.

[36] J. Rossetti, A. G. Khachaturyan, G. Akcay, Y. Ni, *J. Appl. Phys.* **2008**, *103*, 114113.

[37] Y. M. Jin, Y. U. Wang, A. G. Khachaturyan, J. F. Li, D. Viehland, *Phys. Rev. Lett.* **2003**, *91*, 197601.

[38] S. Jesse, *J. Phys. D* **2011**, *44*, 464006.

[39] S. Jesse, R. K. Vasudevan, L. Collins, E. Strelcov, M. B. Okatan, A. Belianinov, A. P. Baddorf, R. Proksch, S. V. Kalinin, *Annu. Rev. Phys. Chem.* **2014**, *65*, 519.

[40] J. Yin, W. Cao, *Appl. Phys. Lett.* **2001**, *79*, 4556.

[41] Q. Li, S. Jesse, A. Tselev, L. Collins, P. Yu, I. Kravchenko, S. V. Kalinin, N. Balke, *ACS Nano* **2015**, *9*, 1848.

[42] Q. Li, Y. Cao, P. Yu, R. K. Vasudevan, N. Laanait, A. Tselev, F. Xue, L. Q. Chen, P. Maksymovych, S. V. Kalinin, N. Balke, *Nat. Commun.* **2015**, *6*, 8985.

[43] R. K. Vasudevan, H. Khassaf, Y. Cao, S. Zhang, A. Tselev, B. Carmichael, M. B. Okatan, S. Jesse, L.-Q. Chen, S. P. Alpay, S. V. Kalinin, N. Bassiri-Gharb, *Adv. Funct. Mater.* **2016**, *26*, 478.

[44] Z. Li, M. Grimsditch, X. Xu, S. Chan, *Ferroelectrics* **1993**, *141*, 313.

[45] O. Y. Loh, H. D. Espinosa, *Nat. Nanotechnol.* **2012**, *7*, 283.

[46] S. A. Cummer, J. Christensen, A. Alu, *Nat. Rev. Mater.* **2016**, *1*, 16001.

[47] N. I. Zheludev, Y. S. Kivshar, *Nat. Mater.* **2012**, *11*, 917.

[48] P. M. Solomon, B. A. Bryce, M. A. Kuroda, R. Keech, S. Shetty, T. M. Shaw, M. Copel, L.-W. Hung, A. G. Schrott, C. Armstrong, M. S. Gordon, K. B. Reuter, T. N. Theis, W. Haensch, S. M. Rossnagel, H. Miyazoe, B. G. Elmegreen, X.-H. Liu, S. Trolier-McKinstry, G. J. Martyna, D. M. Newns, *Nano Lett.* **2015**, *14*, 2391.

[49] J. Lahann, R. Langer, *MRS Bull.* **2005**, *30*, 185.

[50] M. Yoshida, J. Lahann, *ACS Nano* **2008**, *2*, 1101.

[51] L. Chen, *J. Am. Ceram. Soc.* **2008**, *91*, 1835.

[52] Y. Li, S. Hu, Z. Liu, L. Chen, *Appl. Phys. Lett.* **2002**, *81*, 427.

[53] M. J. Haun, E. Furman, S. J. Jang, H. A. McKinstry, L. E. Cross, *J. Appl. Phys.* **1987**, *62*, 333.

[54] A. K. Tagantsev, *Ferroelectrics* **2008**, *375*, 19.

[55] A. K. Tagantsev, *Ferroelectrics* **1986**, *69*, 321.

[56] Y. Zheng, C. H. Woo, *Nanotechnology* **2009**, *20*, 075401.